



HAL
open science

Reaction-induced volume change triggers brittle failure at eclogite facies conditions

Philippe Yamato, Thibault Duretz, M. Baïssset, Cindy Luisier

► **To cite this version:**

Philippe Yamato, Thibault Duretz, M. Baïssset, Cindy Luisier. Reaction-induced volume change triggers brittle failure at eclogite facies conditions. *Earth and Planetary Science Letters*, 2022, 584, pp.117520. 10.1016/j.epsl.2022.117520 . insu-03638866

HAL Id: insu-03638866

<https://insu.hal.science/insu-03638866>

Submitted on 13 Apr 2022

HAL is a multi-disciplinary open access archive for the deposit and dissemination of scientific research documents, whether they are published or not. The documents may come from teaching and research institutions in France or abroad, or from public or private research centers.

L'archive ouverte pluridisciplinaire **HAL**, est destinée au dépôt et à la diffusion de documents scientifiques de niveau recherche, publiés ou non, émanant des établissements d'enseignement et de recherche français ou étrangers, des laboratoires publics ou privés.

1 **Reaction-induced volume change triggers brittle failure at eclogite facies**
2 **conditions**

3

4 **Yamato P.^{1,2,*}, Duretz T.^{3,1}, Baisset M.⁴ and Luisier C^{3,1}.**

5 ¹Univ Rennes, CNRS, Géosciences Rennes - UMR 6118, F-35000 Rennes, France

6 ²Institut Universitaire de France, Paris, France

7 ³Institut für Geowissenschaften, Goethe Universität, 60438 Frankfurt am Main, Germany

8 ⁴Institut des Sciences de la Terre de Paris, Université Pierre et Marie Curie, 75005 Paris, France.

9 *email: philippe.yamato@gmail.com (corresponding author)

10

11

12 **Highlights:**

- 13 - Densification due to eclogitization reaction can generate significant shear stresses
14 - Degree of reaction overstepping impacts the amount of generated shear stresses
15 - Reaction-induced stresses can trigger brittle failure at high-pressure conditions
16 - Negative volume change and associated brittle failure enhance reaction propagation

17

18 **Keywords:**

19 volume change, High-Pressure metamorphism, frictional plasticity, numerical modelling

20

21

22 **Abstract**

23

24 Metamorphic reactions can lead to important changes in rock strength and density. Eclogitization
25 constitutes one of the most emblematic transformations in continental subduction zones, where
26 conversion of lower crustal rocks into eclogite facies rocks correlates with the occurrence of
27 seismogenic events. The relationship between eclogitization and seismicity has been highlighted in
28 several studies, but the processes that trigger brittle failure remain highly debated. Indeed, whether
29 the change in density (from $\sim 2850 \text{ kg.m}^{-3}$ to $\sim 3300 \text{ kg.m}^{-3}$) or the change in rheology can lead to
30 embrittlement is still enigmatic. Here we show that eclogitization-induced volume change occurring
31 out of equilibrium can, by itself, generate sufficient shear stress to fail the rocks at high-pressure
32 conditions. Intermediate-depth earthquakes in continental subduction zones could therefore be
33 explained by volume changes, even without considering rheological modifications induced by
34 mineral reactions. Our results also indicate that interplay between negative volume change and
35 frictional plastic yielding can enhance the propagation of the eclogitization process by a runaway
36 mechanism as long as the reaction is not limited by the lack of reactants.

37

38 **1. Introduction**

39

40 When buried at depth in convergent zones, rocks are subjected to pressure (P) and temperature (T)
41 changes. Depending on their chemical composition and fluid content, the mineral assemblages and
42 proportions evolve toward more thermodynamically stable assemblages at increasing P - T
43 conditions (Spear, 1993). Eclogitization of the oceanic and continental crust involves a large
44 increase in solid density and fluid release, which have significant impacts on tectonic deformation
45 and long-term lithosphere dynamics (e. g., Kirby et al., 1996; Hacker et al., 2003; Jung et al., 2004;
46 Hetenyi et al., 2007; 2021; Malvoisin et al., 2020). In addition, there is growing evidence
47 supporting a genetic link between eclogitization reactions and short-term geological processes, such

48 as the generation of seismic events at intermediate depth (Fig. 1a, b, Hacker et al., 2003; Jung et al.,
49 2004; Austrheim and Boundy, 1994; Hetenyi et al., 2007; Nakajima et al., 2013; Shi et al., 2018;
50 Incel et al., 2019).

51 However, it is still unclear and there is no consensus yet on the mechanism responsible for this
52 behaviour. Indeed, even the strongest mineral phases are expected to deform in a ductile rather than
53 brittle manner above 700°C and 1 GPa of confining pressure, and for a strain rate of 10^{-14} s^{-1} (e.g.
54 dry plagioclase flow laws, Rybacki and Dresen, 2000; 2004). We thus face a chicken-and-egg
55 problem: it is hard to decipher whether brittle deformation is induced by metamorphic reactions or
56 if the reaction itself triggers embrittlement at high pressure. Several studies have addressed this
57 issue by proposing either of these scenarios. On one hand, reaction-induced embrittlement has been
58 proposed to be caused by (i) the change in strength of the newly formed reaction products (grain-
59 size reduction, nucleation and/or growth of weaker phases, Stünitz and Tullis, 2001; John et al.,
60 2009; Thielmann et al., 2015; Incel et al., 2017), (ii) dehydration of the transforming rocks leading
61 to hydrofracturing through a pore fluid pressure increase (Hacker et al., 2003; Jung et al., 2004,
62 Hetényi et al., 2007; 2021; Alvizuri and Hetényi, 2019), and (iii) volume change (McGarr, 1976;
63 Pennington, 1984; Kirby et al., 1996; Malvoisin et al., 2017; 2020). On the other hand, it has been
64 proposed that brittle fracturing could be triggered by transient high stress conditions over very short
65 timescales, leading to external fluid infiltration and subsequent transformation of the granulite into
66 eclogite (e.g., Jamtveit et al., 2018). In the latter case, brittle failure at intermediate depths is
67 induced in response to remote seismic events occurring in the seismogenic zone at shallower levels
68 (Jamtveit et al., 2018), while in the other aforementioned scenarios, brittle failure occurs in situ as a
69 consequence of a reaction-induced stress perturbation. Whatever the mechanism responsible for
70 embrittlement, it is also plausible that the deformation of the lower continental crust results from a
71 cyclic interplay between fracturing-induced reaction and reaction-induced fracturing involving
72 successive stages of fluid pumping and release. Another mechanism that has been proposed to
73 explain embrittlement is volume change. Although embrittlement triggered by diminishing solid

74 density reactions (e. g., serpentinization, melting) has already been suggested (e. g., Kelemen and
75 Hirth, 2012; Vrijmoed et al., 2009; Schmalholz et al., 2020; Malvoisin et al., 2021) and studied
76 using numerical models (Malvoisin et al., 2017; Ulven et al., 2014), densification has received less
77 attention. Moreover, due to complex numerical issues, only recently could frictional plasticity be
78 robustly included into models that account for non-linear visco-elasto-plastic deformation of
79 heterogeneous and compressible materials (e. g., Duretz et al., 2021).

80 Lower crustal rocks consist of amphibolite to granulite facies rocks, whose densification is mainly
81 controlled by the transformation of plagioclase into omphacite (Fig. 1c-e). It is associated with an
82 important density change of $\sim 400\text{-}500 \text{ kg.m}^{-3}$ (Fig. 1f) and with a transient variations of material
83 strength (Bras et al., 2021). Another major characteristic of densification reactions in fluid under-
84 saturated lower crustal rocks, such as amphibolites and granulites, is that they usually take place far
85 from the predicted thermodynamic equilibrium (e.g., Austrheim, 1987; Wayte et al., 1989; Wain et
86 al., 2001; Jackson et al., 2004; Hetényi et al., 2007, 2021). Metastability of such rocks in subduction
87 zones has been discussed in several studies (Lund et al., 2004; Young and Kylander-Clark, 2015;
88 Palin et al., 2017) and fast rock transformation, after a delay corresponding to a reaction overstep of
89 several kbars, has been proposed as a cause of intermediate-depth earthquakes (Dennis and Walker,
90 1965; Jamtveit et al., 2016; Incel et al., 2019; Hetényi et al., 2007; 2021).

91 Here, we investigate the mechanical response to densification of the lower crust using thermo-
92 mechanical numerical modelling. The aim of this study is therefore to quantify the amount of shear
93 stress that can be generated by the solid volume change induced by eclogitization, by taking into
94 account reaction pressure overstepping (Fig. 2 a, b). We consider the eclogitization as a
95 densification reaction and voluntarily ignore the potential strength variations induced by this
96 transformation (i.e. reaction softening/hardening). Our study can then be considered as an end-
97 member case, in which adding a softening mechanism would further amplify strain localisation that
98 is already generated by densification. We show that, in deforming rocks, the stress generated during

99 densification can indeed overcome the yield stress, hence generating frictional plastic yielding in
100 rocks that would otherwise be in the ductile realm.

101

102 **2. Methods**

103 **2.1. Modelling strategy and validation**

104 We designed numerical models to simulate the progress of eclogitization of a radial inclusion
105 enclosed in a granulitic material (Fig. 2c, d) placed at metastable conditions (i.e., at a background
106 pressure (P_{BG}) larger than the pressure of the reaction (P_r) predicted by equilibrium
107 thermodynamics) for a fixed temperature (Fig. 2a, b). The initial degree of overstepping is set by
108 initially placing the whole model at a background pressure of 500 MPa (for the reference model)
109 above the pressure of reaction (i.e., $P_{BG} = 2.0$ GPa and $P_r = 1.5$ GPa).

110 First, a one-dimensional (1D) model (Fig. 2c) involving linear viscous rheology was used to extract
111 the maximum shear stress obtained during the densification of a segment of the model (r_{inc}) placed
112 in metastable conditions (i.e., $P_{BG} > P_r$), assuming no background strain rate (see section 2.3). A
113 constant linear viscous rheology ($\eta = 10^{22}$ Pa.s) is used throughout the model. Parameters are given
114 in Table 1. This model allowed us to perform an intensive parametric study on the following
115 parameters: degrees of overstepping (ΔP_m), density variation ($\Delta\rho$), shapes of density evolution (d_{Pr}),
116 reaction kinetics (τ_k), shear modulus (G), bulk modulus (K), and linear viscosities (η). Results of
117 this parametric study are presented in Supplementary Figure 1.

118 Two-dimensional (2D) models (Fig. 2d), built upon the 1D models, were used to incorporate the
119 effect of background strain rate and to account for visco-elasto-viscoplastic (V-E-VP) rheologies
120 (see section 2.4), allowing to better quantify the amount of brittle failure and its spatial evolution.

121 Both 1D and 2D models were tested against an analytical solution based on the approach of Lee and
122 Tromp (1995; see section 2.2. and Supplementary Figure 2). Matlab scripts to solve the analytical
123 solution and to reproduce the 1D model are provided in the Supplementary Materials. The results of

124 the 1D and 2D models are identical and both converge with increasing grid resolution (see
125 Supplementary Figure 3).

126

127 **2.2. Analytical solution**

128 The analytical solution was developed following the method presented in Lee and Tromp (1995).

129 To allow for a direct comparison with the 2D models, the original solution was modified to account

130 for cylindrical coordinates. Displacement, pressure and stress fields are caused by the instantaneous

131 density change (from ρ_i to ρ_f) of a cylindrical inclusion of radius r_{inc} embedded in an elastic matrix.

132 The associated volume change generates a self-induced stress, which is proportional to the density

133 change through a constant C that can be expressed as:

$$134 \quad C = -\frac{1}{2} \ln \frac{\rho_f}{\rho_i} \quad (1)$$

135 The radial displacement vector (u_r), in cylindrical coordinates, can then be computed analytically

136 for a variable radial distance r using the following equation:

$$137 \quad u_r = Ar - B \frac{1}{2r} \quad (2)$$

138 where A and B , that depend on C , are constants. The latter may be determined from the application

139 of boundary and transmission conditions associated with material interfaces (i.e. inclusion for $r \leq$

140 r_{inc} and matrix for $r > r_{inc}$, see script `SphereInHole_cylindrical.ipynb` for more details). The

141 inclusion and the matrix are both considered elastic with similar material properties (i.e. bulk

142 modulus $K=40$ GPa and shear modulus $G=30$ GPa). However, the proposed analytical solution

143 could also be used for different elastic properties between the reacting inclusion and the matrix. The

144 Matlab script corresponding to this analytical solution is provided in supplementary file

145 (`AnalyticalSolution.m`). It allows to test the validity of both the 1D and the 2D model used in our

146 study (See Supplementary Figure 2).

147

148 **2.3. Description of the 1D model**

149 The 1D model used in this study solves the continuity and momentum equations in the $[r, p]$ polar
 150 coordinates. In this coordinate system, we consider the volume change affecting a radial inclusion
 151 (with a radius r_{inc}) embedded in a radial domain (Fig. 2c). In the absence of body forces and inertia,
 152 the continuity and momentum equations are expressed as:

$$153 \quad \frac{d \ln(\rho)}{dt} = -\frac{1}{r} \frac{\partial(rV_r)}{\partial r} \quad (3)$$

154 and:

$$155 \quad \frac{\partial \sigma_{rr}}{\partial r} + \frac{1}{r} (\sigma_{rr} - \sigma_{pp}) = 0 \quad (4)$$

156 where ρ is the density, V the velocity, r the distance from the center of the model, and σ_{rr} and σ_{pp}
 157 are the normal stress in r and p direction, respectively. By definition, total stresses (σ_{rr} and σ_{pp})
 158 can be decomposed as:

$$159 \quad \begin{cases} \sigma_{rr} = -P + \tau_{rr} \\ \sigma_{pp} = -P + \tau_{pp} \end{cases} \quad (5)$$

160 where P is the pressure and τ_{rr} and τ_{pp} , the deviatoric stresses. Note that here stresses are defined
 161 as negative in compression. Material constituting the inclusion and the matrix are defined with
 162 visco-elastic rheology (see parameters in Table 1) considering a linear viscosity (η) and a shear
 163 modulus (G). Deviatoric stresses can therefore be computed as:

$$164 \quad \begin{cases} \tau_{rr} = 2\eta_{ve} \dot{\epsilon}'_{rr} \\ \tau_{pp} = 2\eta_{ve} \dot{\epsilon}'_{pp} \end{cases}, \quad (6)$$

165 where $\dot{\epsilon}'_{rr}$ and $\dot{\epsilon}'_{pp}$ are the effective deviatoric strain rate components, and η_{ve} corresponds to an
 166 effective visco-elastic modulus expressed as follow:

$$167 \quad \eta_{ve} = \left(\frac{1}{\eta} + \frac{1}{G\Delta t} \right)^{-1}, \quad (7)$$

168 where Δt corresponds to the time step used in the model for time discretisation. The effective visco-
 169 elastic deviatoric strain rate components are expressed as:

$$170 \quad \begin{cases} \dot{\epsilon}'_{rr} = \dot{\epsilon}_{rr} + \frac{\tau_{rr}^0}{2G\Delta t} \\ \dot{\epsilon}'_{pp} = \dot{\epsilon}_{pp} + \frac{\tau_{pp}^0}{2G\Delta t} \end{cases}, \quad (8)$$

171 τ_{rr}^0 and τ_{pp}^0 corresponding to the deviatoric stresses obtained in the previous time step (see Duretz
 172 et al., 2021). The driving force in the model is only controlled by the volume change associated
 173 with the density change. Motion occurs because the initial pressure (P_{BG}) is higher than the pressure
 174 of reaction (P_r). The reaction progress (see Fig. 2b), depends on pressure P and is expressed as a
 175 cumulative distribution function (CDF) and takes the following form:

$$176 \quad X_{eq} = 1 - \frac{1}{2} \left(\operatorname{erfc} \left(\frac{P - P_r}{d_{P_r}} \right) \right) \quad (9)$$

177 where P_r is the ‘‘pressure of reaction’’ (reaction line on Fig. 2a) and d_{P_r} corresponds to a standard
 178 deviation of the CDF controlling the density change sharpness (Fig. 2b). At a given P , the value of
 179 X_{eq} computed using (9) therefore corresponds to a value at equilibrium. In order to introduce a
 180 reaction kinetics, the value of X considered is computed implicitly using:

$$181 \quad \frac{dX}{dt} = \frac{X_{eq} - X}{t_k} \quad (10)$$

182 t_k being the kinetic parameter that defines the characteristic reaction time. The reference density is
 183 then computed at each time step as:

$$184 \quad \rho_0 = X\rho_{0f} + (1 - X)\rho_{0i} \quad (11)$$

185 where ρ_{0i} and ρ_{0f} corresponds to the initial reference density (2850 kg.m⁻³ for the granulite) and
 186 the final reference density (3250 kg.m⁻³ for the eclogite), respectively. Density introduced in
 187 continuity equation includes pressure dependency and therefore corresponds to:

$$188 \quad \rho = \rho_0 \exp(\beta P) \quad (12)$$

189 where $\beta = 1/K$, is the compressibility (see Table 1). Note that thermal expansivity is not considered
 190 and temperature is kept constant throughout the simulations. At each time step, the equations (3-4)
 191 are discretized using a staggered finite difference scheme and solved using a pseudo-transient
 192 solving strategy (e.g. Duretz et al., 2019). The mesh is advected in a Lagrangian manner following
 193 the obtained velocity field. The Matlab script corresponding to this code is provided in
 194 supplementary file (Numerics1D_polar.m). It allows to run the 1D reference model and can thus be
 195 used to reproduce Figures 3g-i.

196

197 **2.4. Description of the 2D model**

198 The 2D thermo-mechanical simulations were carried out using the code MDoodz6.0, which
199 accounts for a V-E-VP rheological model (Duretz et al., 2021). The continuity and momentum
200 equations are solved in 2D Cartesian $[x,y]$ coordinates, neglecting both gravity and inertial terms,
201 such as:

$$202 \quad \frac{d \ln(\rho)}{dt} = -\frac{\partial v_i}{\partial x_i} \quad (13)$$

$$203 \quad \frac{\partial \sigma_{ij}}{\partial x_j} = 0 \quad (14)$$

204 The heat transfer equation is expressed as:

$$205 \quad \rho C_p \frac{DT}{Dt} = \frac{\partial}{\partial x_i} \left(k \frac{\partial T}{\partial x_i} \right) + Q_s \quad (15)$$

206 where k is the conductivity and C_p the heat capacity. Q_s corresponds to viscoplastic dissipation.
207 Note that heat transfer does not affect our results: the temperature remains constant at the
208 considered spatio-temporal scale.

209 The partial differential equations are discretised using a staggered finite difference scheme and
210 markers-in-cell method (Gerya and Yuen, 2003). The non-linear mechanical equations are solved
211 using a full Newton-Raphson method with analytical derivation of the Jacobian (see Duretz et al.,
212 2021). Successive Newton corrections are computed using a direct-iterative scheme that relies on
213 Powell-Hestenes iterations, Cholesky factorization of the symmetrised Jacobian operator and
214 Generalized Conjugate Residual (Räss et al., 2017). The optimal Newton step is computed via a
215 direct line-search globalization procedure (Duretz et al., 2015). Marker positions are evolved
216 forward in time using a fourth order (in space) Runge-Kutta scheme. The Courant number is set to
217 0.2. The implementation of the V-E-VP rheological model follows Yamato et al. (2019) and Duretz
218 et al. (2021). The contribution of each deformation mechanism is computed iteratively to satisfy the
219 following Maxwell model (e.g., Popov & Sobolev, 2008):

$$220 \quad \dot{\epsilon}_{ij} = \dot{\epsilon}_{ij}^v + \dot{\epsilon}_{ij}^e + \dot{\epsilon}_{ij}^{vp} \quad (16)$$

221 where the v, e and vp superscripts refer to the viscous, elastic, and visco-plastic (frictional)
 222 contributions to the total strain rate. In contrast to the 1D model, a dislocation creep flow law is
 223 considered in the 2D model. The flow stress (τ_v) is thus stress and thermal dependent and is
 224 expressed as:

$$225 \quad \tau_v = 2F_{\text{pwl}}A^{-\frac{1}{n}}\exp\left(\frac{Q}{nRT}\right)\dot{\epsilon}_{\text{II}}^{\frac{1}{n}} \quad (17)$$

226 where n , A , and Q are the dislocation creep parameters of the material (see Table 1) and R is the
 227 universal gas constant ($R = 8.314510 \text{ J}\cdot\text{K}^{-1}\cdot\text{mol}^{-1}$). F_{pwl} corresponds to the correction factor (e.g.,
 228 Schmalholz & Fletcher, 2011) for invariant formulation relative to the type of experiments used for
 229 calibration (here axial compression), such as:

$$230 \quad F_{\text{pwl}} = \frac{1}{6}2^{\frac{1}{n}}3^{\frac{n-1}{2n}}. \quad (18)$$

231 In contrast to the 1D simulations, the 2D simulations include the effect of frictional rheology. To
 232 this end a viscoplastic Drucker-Prager rheological model is employed³⁵. The yield function is
 233 expressed as:

$$234 \quad F = \tau_{\text{II}} - P \sin \varphi - C \cos \varphi - 2\eta_{\text{vp}}\dot{\epsilon}_{\text{II}}^{\text{vp}} \quad (19)$$

235 where τ_{II} is the deviatoric second stress invariant, P is the pressure, C is the cohesion and φ is the
 236 friction angle. The viscoplastic parameter, η_{vp} , is set such that the overstress ($2\eta_{\text{vp}}\dot{\epsilon}_{\text{II}}^{\text{vp}}$) is on the
 237 order of 0.1 MPa (i.e. $\eta_{\text{vp}} = 5 \times 10^{18} \text{ Pa}\cdot\text{s}$ for $\dot{\epsilon}_{\text{BG}} = 10^{-14} \text{ s}^{-1}$) in our simulations. Tests of convergence
 238 for 2D models involving plasticity can be found in Supplementary Figure 5. The effect of plastic
 239 dilation is neglected and the plastic flow potential (Q) thus simply reads as $Q = \tau_{\text{II}}$. The reaction
 240 progress law and reaction kinetics are included in a similar manner as in the 1D code described
 241 above (see eq. 9 to 12).

242

243 **2.5. Choice of parameters for reference models**

244 In this study, eclogitization is restricted to a progressive densification process (Fig. 2b). The choice
245 of parameters for defining a reference model is based on data from granulite to eclogite
246 transformation, that has been intensively studied in the Bergen Arcs. Based on recent chemical data
247 and P - T estimates performed in Holsnøy (Bhowany et al., 2018), we set P_r for the granulite to
248 eclogite transformation at 1.5 GPa for a temperature of 680°C. A d_{P_r} value of 700 MPa was chosen
249 as it seems to be in good agreement with the density evolution that encompass several reactions
250 occurring with a P increase (Bras et al., 2021, Fig. 1f). Thermodynamic modelling providing the
251 Fig.1f was performed using Perple_X_6.9.1 (Connolly 1990; 2009) and the internally consistent
252 thermodynamic database hp62ver.dat (Holland and Powell, 2011). The solution models are for
253 feldspar (Furhman and Lindsley, 1988), garnet (White et al., 2014), clinopyroxene (Green et al.,
254 2007), clinoamphibole (Green et al., 2016), epidote (Holland and Powell, 2011), white mica (White
255 et al., 2014), and melt (Green et al., 2016). Bulk composition used corresponds to sample
256 HOL7C_2014 (Bhowany et al., 2018). A difference in density of 400 kg.m⁻³ using a reference
257 density of 2850 kg.m⁻³ for the granulite ($X=0$) and of 3250 kg.m⁻³ for the eclogite ($X=1$) appears
258 also in good agreement with previous studies (Austrheim 1987; Hetenyi et al., 2007). The kinetic
259 parameter t_k has been fixed to 100 yrs as there are arguments that granulite to eclogite
260 transformation is rather a fast process (Malvoisin et al., 2020). The choice of the anorthite dry
261 (Rybacki and Dresen, 2000) was stimulated by the fact that initial material corresponds to dry
262 granulite. K and G values (Motra and Zertani, 2018). For 2D model involving plasticity, cohesion
263 and friction angle were set to 50 MPa and 30°, as they correspond to an extrapolation of Byerlee's
264 (1978) data at high pressure. The strain rate used in the 2D reference model is 10⁻¹⁴ s⁻¹.

265

266 **3. Results**

267 **3.1. Results from the reference model**

268 Figure 3 displays the results obtained in absence of background strain rate and for a linear viscosity
269 set to 10²² Pa.s. It shows that reaction-induced volume change affects both shear stress and pressure

270 fields. Shear stresses (τ_{II}) generated by the negative volume change of the inclusion are distributed
271 in a radial configuration around the inclusion (Fig. 3a-c). A fast, transient and important shear stress
272 increase, larger than 500 MPa, occurs in the vicinity of the reacting area at a time close to the onset
273 of reaction (Fig. 3a). After reaching a maximum value (here of ~ 0.6 GPa), shear stresses then
274 decrease following a Maxwell-type relaxation (Dabrowski et al., 2015) until they become null once
275 equilibrium density is reached.

276 Simultaneously, the densification reaction induces a pressure decrease in both the matrix and the
277 inclusion (Fig. 3 d-f). In the inclusion, there is first a rapid pressure drop (see Fig. 3d compared to
278 the 2.0 GPa initial pressure in both inclusion and matrix, and green line in Fig. 3g-h), followed by a
279 consecutive pressure increase to reach the same pressure as in the matrix (Fig. 3g, h). The pressure
280 decrease in the matrix is smoother (black line in Fig. 3g-h). It is associated to the increase in matrix
281 volume accommodating the shrinking of the inclusion, to satisfy mass conservation. An important
282 point to note is that the reaction stops as soon as both the inclusion and the matrix reached the same
283 density, since our model is only driven by density change, which is not necessarily the one
284 predicted for the reaction to be complete (i.e., $X=1$).

285 As the value of the maximum shear stress reached ($\max(\tau_{II})$) constitutes a useful metric that
286 indicates whether reaction-induced volume change can lead to rock failure, we have tracked this
287 value through a complete parametric study (see Supplementary Figure 1). Figure 4a shows the
288 effect of pressure overstepping and density change associated to the metamorphic reaction on the
289 value of $\max(\tau_{II})$. The results show that density variations produce shear stress. They also show that
290 when a metamorphic reaction is associated with a change in density larger than a few tens of $\text{kg}\cdot\text{m}^{-3}$,
291 pressure overstepping always leads to shear stress generation, and that the larger the density change
292 is, the higher the effect of the overstepping is.

293 The proportion of reacting material is also a key factor (Fig. 4b). Maximum shear stress is reached
294 when the amount of initial reacting material is small ($<10\%$) in comparison to the total amount of

295 material. If the initial reacting area is higher than 20-30%, the maximum shear stress reached is
296 much less important.

297

298 **3.2. Influence of densification on frictional plastic shear banding**

299 The mechanical consequences of volume changes in an isoviscous host-inclusion system are
300 different from that in host-inclusion systems involving viscosity contrasts and subjected to shear
301 (e.g. Schmid and Podladchikov, 2003; Moulas et al., 2014, Luisier et al., 2019). Figure 5 compares
302 pressure and shear stress fields obtained for models including reaction-induced volume change (Fig.
303 5a, b) with models involving a viscosity ratio of 1000 between inclusion and matrix (Fig. 5 c, d),
304 under a background strain rate of 10^{-14} s^{-1} .

305 In Figure 5a, inclusion and matrix have the same viscosity and frictional plasticity is not activated.
306 In this case, there is no significant change in pressure around the inclusion. The shear stress (τ_{II})
307 generated by the negative volume change of the inclusion is radial (see Fig. 3a), but because of the
308 pure shear background strain rate (horizontal shortening and vertical stretching), the shear stress
309 field is different in vertical and horizontal direction. τ_{II} values are higher in the vertical direction
310 where shear stresses due to the volume change and shear stresses due to stretching are in the
311 opposite sense. For the same reason, τ_{II} values are smaller in the horizontal direction where
312 shortening accompanies the shrinking of the inclusion. When frictional plasticity (i.e. pressure
313 dependent) is accounted for (Fig. 5b), we observe that plastic yield stress in matrix is reached in the
314 area undergoing stretching (where τ_{II} values are high) whereas it is not reached in the area
315 undergoing shortening (where τ_{II} values are low). The regions undergoing plastic deformation
316 (contoured in white in Fig. 5b) are located close to the reacting inclusion in the stretching direction.
317 Figure 5c displays pressure and shear stress field obtained for a model using the same parameters as
318 in Fig. 5a, except that (i) there is no volume change and (ii) inclusion and matrix have different
319 viscosities (viscosity 1000 times weaker in the inclusion). In this case, the shear stress field is
320 identical in vertical and horizontal directions, but the pressure field is not. Due to the presence of a

321 weak inclusion, a pressure increase occurs in the matrix close to the inclusion in the vertical
322 direction (parallel to stretching). In the horizontal direction, the pressure decreases. Pressure and
323 shear stress fields are therefore drastically different than in the previous case involving volume
324 changes without viscosity contrast. In the “viscosity-contrast” case, shear stress is maximum where
325 the pressure is the lowest in the matrix, close to the inclusion in horizontal direction. These areas
326 constitute favourable locations for frictional plastic yielding. In the vertical direction, because of
327 locally higher pressure values, a larger shear stress is required to reach the yielding. This is the
328 reason why the parts undergoing plastic deformation (white contours in Fig. 5d) are located close to
329 the reacting inclusion in the shortening direction, in the case where plasticity is switched on.
330 In Figure 5, viscosities are considered stress dependent with a stress exponent $n=3$. Even if n is
331 known to affect relaxation time and pressure evolution (Dabrowski et al., 2015), performing the
332 same models considering a constant viscosity with $n=1$ does not drastically change the results
333 concerning matrix deformation over the considered time scale (see Supplementary Figure 4).

334

335 **3.3. Brittle failure in ductile realm**

336 Our results show that depending on ΔP_m , the amount of shear stress produced ($\max(\tau_{II})$) by
337 considering only reaction-induced volume change is significant (Fig. 4). For a given material, at a
338 fixed pressure-temperature-strain rate (P - T - $\dot{\epsilon}$) conditions in the ductile field, shear stress (τ_v)
339 supported by this material is below the yield stress value (τ_y) required to fail (Fig. 6a). By
340 definition, this difference in stress $\Delta\tau$ (with $\Delta\tau = \tau_y - \tau_v$) can be overcome by (1) increasing strain
341 rate, (2) decreasing pressure and/or (3) decreasing temperature. We here show that shear stresses
342 resulting from reaction-induced volume change can also overcome $\Delta\tau$ and thus trigger yielding. The
343 occurrence of ductile and brittle deformation is therefore strongly linked to volume changes
344 associated with metamorphic reactions.

345 Figure 6b displays the value of $\Delta\tau$ as a function of P and $\dot{\epsilon}$ for dry anorthite (Rybacki and Dresen,

2000). $\Delta\tau$ isocontours are presented in black. The brittle-ductile transition (BDT, yellow line) corresponds to $\Delta\tau = 0$. Conditions of the parametric study performed for different degrees of overstepping (right vertical axis) and different background strain rates considering a density difference $\Delta\rho$ of 400 kg.m^{-3} (i.e., roughly as in the granulite to eclogite transformation) are also presented (see symbols). White lines correspond to isovalues of the amount of anorthite matrix that undergone brittle failure in case of reaction-induced volume change. An illustration of the effect of the background strain rate is presented in Fig. 6c-g. Results show that the field where yield stress is achievable due to reaction-induced volume change covers a large part of the domain where ductile deformation is expected for dry anorthite if metamorphic transformation were not activated (Fig. 6b). By accounting for the stress induced by volume change, the position of the brittle-ductile boundary can be shifted towards lower strain rate values, reducing the required strain rate necessary to fail the rock up to two orders of magnitude. Destabilization of a ductile metastable granulite into eclogite anywhere in this domain can lead to brittle failure.

4. Discussion and conclusion

Our results show that eclogitization-induced densification occurring under metastable conditions can, by itself, generate sufficient shear stress to fail the rocks at high-pressure conditions. Brittle failure in rocks can therefore be explained by densification reactions, without even considering the rheological changes induced by the reaction. In light of these results, it is now possible to further discuss the applicability of our model on natural cases and the broader implications of this study on the strength of the continental lithosphere subjected to metamorphic reactions. These points will be addressed in the following, after a discussion on possible perspectives concerning our modelling approach.

4.1. Modelling perspectives

In the present study we intentionally did not consider the potential rheological changes associated with the metamorphic transformation. Modification of strength is transient and only caused by

371 densification. This choice has been made to isolate and study in detail the effect of densification
372 alone. One important consequence of this is the value of pressure obtained in the transforming area,
373 which is lower than the pressure in the unreacted matrix. However, in models considering only
374 strength difference between inclusion and matrix (as in Fig. 5c, d), the weaker the inclusion is
375 compared to its matrix, the higher the pressure difference will be between the inclusion and matrix
376 (Schmid and Podladchikov, 2003; Moulas et al., 2014, Luisier et al., 2019). We can therefore
377 speculate that by taking into account a viscosity decrease of the inclusion in addition to volume
378 change during the transformation would lead to higher pressure inside the inclusion compared to
379 models that only consider volume changes. Depending on the magnitude of such a viscosity
380 decrease, the pressure inside the inclusion could even be higher than the pressure in the surrounding
381 matrix. In such a case, this pressure increase would extend the degree of overstepping of the rock.
382 This is something that can be expected for the eclogitization process in specific cases, such as the
383 granulite to eclogite transformation, as it is classically proposed that the eclogite is weaker, at least
384 transiently, than its granulitic protolith (Labrousse et al., 2010; Bras et al., 2021; Kaatz et al., 2021).

385 Our models assume that the third direction of space is infinite. Our analytical solution (see section
386 2.2) shows that the stresses induced by volume change (“self-induced stresses”) in cylindrical
387 coordinates corresponds to 2/3 of the self-induced stresses obtain in spherical coordinates (Lee and
388 Tromp, 1995; Gillet et al., 1984). Hence, considering the eclogitization process in 3D would
389 therefore lead to higher self-induced stresses than in 2D. In that sense, our estimates of the ability to
390 reach brittle failure can then be taken as minimum.

391 We assume conservation of mass and thus consider a closed system. A variation of density therefore
392 only impacts volume change. However, it is well known that any replacement reaction, whether it is
393 a volume increase or reduction, involves the formation of intra-crystalline porosity along with the
394 product minerals, as evidenced by pseudomorph microtextures (Putnis, 2002; 2009; 2015). In the
395 case of an open system subjected to input of externally derived fluids, such a porosity can be filled
396 by product minerals, thus limiting or even inhibiting the volume change (Centrella et al., 2015).

397 Similarly, mineral replacement can occur via a process of isovolumetric interface-coupled
398 dissolution-precipitation during open system fluid-rock interaction (Putnis, 2009; Centrella et al.,
399 2015). From this point of view, our model constitutes an end-member that can however be applied
400 in cases where mass balance is fulfilled (Centrella et al., 2018).

401 **4.2. Applications and Implications**

402 The degree of overstepping a rock can sustain before reacting plays a major role on its mechanical
403 behaviour. Indeed, our results show that it extends the brittle field toward lower strain rate values
404 (Fig. 6). Many examples have been reported where the plagioclase breakdown reaction is thought to
405 have been inhibited because of the lack of free fluid (Austrheim, 1987; Wayte et al., 1989; Rubie,
406 1998; Jackson et al., 2004; Young and Kylander-Clark, 2015; Jamtveit et al., 2016; Palin et al.,
407 2017). The preservation of metastable plagioclase at high pressure can generate pressure
408 overstepping of the order of several 100's of MPa as already suggested by Wayte et al. (1989) for
409 the Allalin metagabbro (Alps) and Hetényi et al. (2007; 2021) for the Indian lower crust (beneath
410 the Tibetan Plateau), and sometimes up to pressure higher than 1.0 GPa (e.g., Wain et al., 2001).
411 Densification of rocks triggered by mineral reactions that take place far from the equilibrium
412 constitutes therefore a mechanism for explaining the nucleation of mechanical instabilities at depth
413 during the burial of a dry continental lithosphere and it is in good agreement with kinetics laws (e.g.
414 Cahn, 1956). In the case of a densification reaction such as the eclogitization of plagioclase-bearing
415 rocks (e.g. Norwegian or Himalayan granulites, Alpine gabbros), it is hence appropriate to study the
416 effects of volume change on the initiation of such instabilities.

417 Assessing the seismic potential of such a failure occurring at intermediate depth in continental
418 subduction zones is challenging and remains under the scope of this study. The question regarding
419 their potential seismogenic nature remains open and could be answered by using dynamic rupture
420 models (Gabriel et al., 2020, Thomas and Bhat, 2018) and/or laboratory experiments (Schubnel et
421 al., 2013).

422 Our results also show that the mechanical effect of reaction-induced volume change on deformation
423 is important even if only a small amount of material is transformed. Reaction-induced shear stress is
424 indeed maximum when the initial amount of material allowed to react is small (<10%, see Fig. 4b).
425 Maximum shear stress values then gently decrease when the ratio between the initial volume of
426 reacting material and total volume of rocks increase (Vol_{inc}/Vol_{tot} in Fig. 4b), reaching a plateau of
427 low shear stresses for values of $Vol_{inc}/Vol_{tot} \sim 30-40\%$. This is in good agreement with the absence
428 of seismicity observed in subducting continental crust where eclogitization progress exceed 30-40%
429 (see Fig. 1a, b). This could explain why pseudotachylytes are only observed in partially transformed
430 granulites from Holsnøy (Fig. 1d-f), where the percentage of eclogitization is below $\sim 40\%$ (Boundy
431 et al., 1992).

432 In addition, our results show that even if frictional yielding is reached, the amount of material that
433 undergoes plastic deformation is generally low (i.e., in the order of 1% or less, see Fig. 6).
434 However, this should not be overlooked. When yielding occurs, the pressure in the damaged area
435 drops. In contrast, pressure increases at the tip of the area that has undergone plastic deformation
436 (Fig. 5b). The development of such a pressure gradient could be responsible for a transfer of fluid
437 that may favourably circulate through the damaged zone. Because transformation of granulite into
438 eclogite is mainly driven by the presence of fluids, we can speculate that, if even a small amount of
439 fluid is present in the granulite, it will favourably be collected toward the damage zone and then
440 allow transformation of this area. Figure 7 displays a model where this hypothesis is tested, by
441 allowing areas that have undergone plastic deformation to react (i.e., by allowing density change as
442 it is the case for the initial reacting inclusion). It illustrates progressive eclogitization by a runaway
443 mechanism, which lasts as long as the reaction is not limited by the lack of reactive product. In that
444 case, eclogitization of the granulite self-propagates in the direction perpendicular to the shortening
445 direction, forming finger-like structure of eclogitized material as described in the Holsnøy area
446 (e.g., so-called "static eclogites", Putnis, 2021; Zertani et al., 2019, Jamtveit et al., 2000; 2016).

447 This study has therefore strong implications for our understanding of the state of stress of the

448 continental lithosphere in convergence zones. In such geodynamic contexts, rocks buried at depth
449 are mainly subjected to metamorphic reactions leading to an increase in density. Our results show
450 that the nucleation of brittle instabilities due to the densification reaction taking place far from
451 equilibrium can generate important transient stresses, hence extending the domain where frictional
452 plastic yielding can occur.

453 **References:**

- 454 Alvizuri, C., & Hetényi, G. Source mechanism of a lower crust earthquake beneath the Himalayas
455 and its possible relation to metamorphism. *Tectonophysics*, **769**, 128153 (2019).
- 456 Austrheim, H. Eclogitization of lower crustal granulites by fluid migration through shear zones.
457 *Earth and Planetary Science Letters*, **81**(2-3), 221-232 (1987).
- 458 Austrheim, H., & Boundy, T. M. Pseudotachylytes generated during seismic faulting and
459 eclogitization of the deep crust. *Science*, **265**(5168), 82-83 (1994).
- 460 Bhowany, K., et al. Phase equilibria modelling constraints on P–T conditions during fluid catalysed
461 conversion of granulite to eclogite in the Bergen Arcs, Norway. *Journal of Metamorphic Geology*,
462 **36**(3), 315-342 (2018).
- 463 Bjørnerud, M., & Magloughlin, J. F. Pressure-related feedback processes in the generation of
464 pseudotachylytes. *Journal of Structural Geology*, **26**(12), 2317-2323 (2004).
- 465 Boundy, T. M., Fountain, D. M., & Austrheim, H. Structural development and petrofabrics of
466 eclogite facies shear zones, Bergen Arcs, western Norway: implications for deep crustal
467 deformational processes. *Journal of Metamorphic Geology*, **10**(2), 127-146 (1992).
- 468 Bras, E., Bâisset, M., Yamato, P., & Labrousse, L. Transient weakening during the granulite to
469 eclogite transformation within hydrous shear zones (Holsnøy, Norway). *Tectonophysics*, 229026
470 (2021).

471 Byerlee, J. Friction of rocks. In *Rock friction and earthquake prediction* (pp. 615-626). Birkhäuser,
472 Basel (1978).

473 Cahn, J.W. The kinetics of grain boundary nucleated reactions. *Acta Metall.* **4**, 449–459.

474 Centrella, S., Austrheim, H., & Putnis, A. Coupled mass transfer through a fluid phase and volume
475 preservation during the hydration of granulite: An example from the Bergen Arcs, Norway. *Lithos*,
476 **236**, 245-255 (2015).

477 Centrella, S., Putnis, A., Lanari, P., & Austrheim, H. Textural and chemical evolution of pyroxene
478 during hydration and deformation: a consequence of retrograde metamorphism. *Lithos*, **296**, 245-
479 264 (2018).

480 Connolly, J. A. D. Multivariable phase diagrams; an algorithm based on generalized
481 thermodynamics. *American Journal of Science*, **290** (6), 666-718 (1990).

482 Connolly, J. A. D. The geodynamic equation of state: what and how. *Geochemistry, Geophysics,*
483 *Geosystems*, **10** (10) (2009).

484 Dabrowski, M., Powell, R., & Podladchikov, Y. Viscous relaxation of grain- scale pressure
485 variations. *Journal of Metamorphic Geology*, **33**(8), 859-868 (2015).

486 Dennis, J. G., & Walker, C. T. Earthquakes resulting from metastable phase
487 transitions. *Tectonophysics*, **2** (5), 401-407 (1965).

488 Duretz T., Schmalholz S. M., & Podladchikov Y. Y. Shear heating-induced strain localisation
489 across the scales, *Philosophical Magazine*, **95** (28-30), 3192-3207 (2015).

490 Duretz T., Räss L., Podladchikov Y. Y. & Schmalholz S. M. Resolving thermomechanical coupling
491 in two and three dimensions: spontaneous strain localization owing to shear heating, *Geophysical*
492 *Journal International*, **216** (1), 365–379 (2019).

493 Duretz, T., de Borst, R., & Yamato, P. Modeling Lithospheric Deformation Using a Compressible
494 Visco- Elasto- Viscoplastic Rheology and the Effective Viscosity Approach. *Geochemistry,*
495 *Geophysics, Geosystems*, **22**(8), e2021GC009675 (2021).

496 Fuhrman, M. L., & Lindsley, D. H. Ternary-feldspar modeling and thermometry. *American*
497 *mineralogist*, **73**(3-4), 201-215 (1988).

498 Gabriel, A. A., Li, D., Chiocchetti, S., Tavelli, M., Peshkov, I., Romenski, E., & Dumbser, M.. A
499 unified first-order hyperbolic model for nonlinear dynamic rupture processes in diffuse fracture
500 zones. *Philosophical Transactions of the Royal Society A*, **379**(2196), 20200130 (2021).

501 Gerya, T. V., & Yuen, D. A. Characteristics-based marker-in-cell method with conservative finite-
502 differences schemes for modeling geological flows with strongly variable transport properties.
503 *Physics of the Earth and Planetary Interiors*, **140**(4), 293-318 (2003).

504 Gillet, P., Ingrin, J., & Chopin, C. Coesite in subducted continental crust: PT history deduced from
505 an elastic model. *Earth and Planetary Science Letters*, **70**(2), 426-436 (1984).

506 Green, E., Holland, T., Powell, R. An order-disorder model for omphacitic pyroxenes in the system
507 jadeite-diopside-hedenbergite-acmite, with applications to eclogitic rocks. *Am. Mineral.* **92**, 1181–
508 1189 (2007).

509 Green, E., White, R., Diener, J., Powell, R., Holland, T., Palin, R. Activity–composition relations
510 for the calculation of partial melting equilibria in metabasic rocks. *J. Metamorph. Geol.* **34**, 845–
511 869 (2016).

512 Hacker, B. R., Peacock, S. M., Abers, G. A., & Holloway, S. D. Subduction factory 2. Are
513 intermediate-depth earthquakes in subducting slabs linked to metamorphic dehydration
514 reactions?. *Journal of Geophysical Research: Solid Earth*, **108** (B1) (2003).

515 Hetényi, G., Cattin, R., Brunet, F., Bollinger, L., Vergne, J., Nábělek, J. L., & Diament, M. Density

516 distribution of the India plate beneath the Tibetan plateau: Geophysical and petrological constraints
517 on the kinetics of lower-crustal eclogitization. *Earth and Planetary Science Letters*, **264** (1-2), 226-
518 244 (2007).

519 Hetényi, G., Chanard, K., Baumgartner, L. P., & Herman, F. Metamorphic transformation rate over
520 large spatial and temporal scales constrained by geophysical data and coupled modelling. *Journal of*
521 *Metamorphic Geology* (2021).

522 Holland, T. J. B., & Powell, R. An improved and extended internally consistent thermodynamic
523 dataset for phases of petrological interest, involving a new equation of state for solids. *Journal of*
524 *metamorphic Geology*, **29**(3), 333-383 (2011).

525 Incel, S., et al. Laboratory earthquakes triggered during eclogitization of lawsonite-bearing
526 blueschist. *Earth and Planetary Science Letters*, **459**, 320-331 (2017).

527 Incel, S., et al. Reaction-induced embrittlement of the lower continental crust. *Geology*, **47** (3), 235-
528 238 (2019).

529 Jackson, J. A., Austrheim, H., McKenzie, D., & Priestley, K.. Metastability, mechanical strength,
530 and the support of mountain belts. *Geology*, **32**(7), 625-628 (2004).

531 Jamtveit, B., Austrheim, H., & Malthe-Sørenssen, A. Accelerated hydration of the Earth's deep
532 crust induced by stress perturbations. *Nature*, **408** (6808), 75-78 (2000).

533 Jamtveit, B., Austrheim, H., & Putnis, A. Disequilibrium metamorphism of stressed
534 lithosphere. *Earth-Science Reviews*, **154**, 1-13 (2016).

535 Jamtveit, B., Ben-Zion, Y., Renard, F., & Austrheim, H. Earthquake-induced transformation of the
536 lower crust. *Nature*, **556**(7702), 487-491 (2018).

537 John, T., Medvedev, S., Rüpke, L. H., Andersen, T. B., Podladchikov, Y. Y., & Austrheim, H.

538 Generation of intermediate-depth earthquakes by self-localizing thermal runaway. *Nature*
539 *Geoscience*, **2** (2), 137-140 (2009).

540 Jung, H., Green II, H. & Dobrzhinetskaya, L. Intermediate-depth earthquake faulting by
541 dehydration embrittlement with negative volume change. *Nature* **428**, 545–549 (2004).

542 Kaatz, L., Zertani, S., Moulas, E., John, T., Labrousse, L., Schmalholz, S.M., & Andersen, T. B.
543 Widening of hydrous shear zones during incipient eclogitization of metastable dry and rigid lower
544 crust – holsnøy, western Norway. *Tectonics*, **40**, e2020TC006572, (2021)

545 Kelemen, P. B., & Hirth, G. Reaction-driven cracking during retrograde metamorphism: Olivine
546 hydration and carbonation. *Earth and Planetary Science Letters*, **345**, 81-89 (2012).

547 Kirby, S. H., Stein, S., Okal, E. A., & Rubie, D. C. Metastable mantle phase transformations and
548 deep earthquakes in subducting oceanic lithosphere. *Reviews of geophysics*, **34**(2), 261-306 (1996).

549 Lee, J. K., & Tromp, J. Self- induced fracture generation in zircon. *Journal of Geophysical*
550 *Research: Solid Earth*, **100**(B9), 17753-17770 (1995).

551 Lund, M. G., Austrheim, H., & Erambert, M. Earthquakes in the deep continental crust-insights
552 from studies on exhumed high-pressure rocks. *Geophysical Journal International*, **158** (2), 569-576
553 (2004).

554 Labrousse, L., Hetényi, G., Raimbourg, H., Jolivet, L., & Andersen, T. B. Initiation of crustal-scale
555 thrusts triggered by metamorphic reactions at depth: Insights from a comparison between the
556 Himalayas and Scandinavian Caledonides. *Tectonics*, **29** (5) (2010).

557 Luisier, C., Baumgartner, L., Schmalholz, S. M., Siron, G., & Vennemann, T. Metamorphic
558 pressure variation in a coherent Alpine nappe challenges lithostatic pressure paradigm. *Nature*
559 *communications*, **10** (1), 1-11 (2019).

560 Malvoisin, B., Podladchikov, Y. Y., & Myasnikov, A. V. Achieving complete reaction while the
561 solid volume increases: A numerical model applied to serpentinisation. *Earth and Planetary
562 Science Letters*, **563**, 116859 (2021).

563 Malvoisin, B., Austrheim, H., Hetényi, G., Reynes, J., Hermann, J., Baumgartner, L. P., &
564 Podladchikov, Y. Y. Sustainable densification of the deep crust. *Geology*, **48**(7), 673-677 (2020).

565 Malvoisin, B., Brantut, N., & Kaczmarek, M. A. Control of serpentinisation rate by reaction-
566 induced cracking. *Earth and Planetary Science Letters*, **476**, 143-152 (2017).

567 McGarr, A. Seismic moments and volume changes. *Journal of geophysical research*, **81**(8), 1487-
568 1494 (1976).

569 Monsalve, G., McGovern, P., & Sheehan, A. Mantle fault zones beneath the Himalayan collision:
570 Flexure of the continental lithosphere. *Tectonophysics*, **477** (1-2), 66-76 (2009).

571 Monsalve, G., Sheehan, A., Schulte-Pelkum, V., Rajaure, S., Pandey, M. R., & Wu, F. Seismicity
572 and one-dimensional velocity structure of the Himalayan collision zone: Earthquakes in the crust
573 and upper mantle. *Journal of Geophysical Research: Solid Earth*, **111** (B10) (2006).

574 Motra, H. B., & Zertani, S. Influence of loading and heating processes on elastic and geomechanical
575 properties of eclogites and granulites. *Journal of Rock Mechanics and Geotechnical
576 Engineering*, **10** (1), 127-137 (2018).

577 Moulas, E., Burg, J. P., & Podladchikov, Y. Stress field associated with elliptical inclusions in a
578 deforming matrix: Mathematical model and implications for tectonic overpressure in the
579 lithosphere. *Tectonophysics*, **631**, 37-49 (2014).

580 Nakajima, J., Uchida, N., Shiina, T., Hasegawa, A., Hacker, B. R., & Kirby, S. H. Intermediate-
581 depth earthquakes facilitated by eclogitization-related stresses. *Geology*, **41**(6), 659-662 (2013).

582 Palin, R. M., Reuber, G. S., White, R. W., Kaus, B. J., & Weller, O. M. Subduction metamorphism
583 in the Himalayan ultrahigh-pressure Tso Moriri massif: an integrated geodynamic and petrological
584 modelling approach. *Earth and Planetary Science Letters*, **467**, 108-119 (2017).

585 Pennington, W. D. The effect of oceanic crustal structure on phase changes and subduction.
586 *Tectonophysics*, 102(1-4), 377-398 (1984).

587 Popov, A. A., & Sobolev, S. V. SLIM3D: A tool for three-dimensional thermomechanical modeling
588 of lithospheric deformation with elasto-visco-plastic rheology. *Physics of the earth and planetary*
589 *interiors*, **171**(1-4), 55-75 (2008).

590 Putnis, A. Mineral replacement reactions: from macroscopic observations to microscopic
591 mechanisms. *Mineralogical Magazine*, **66** (5), 689-708 (2002).

592 Putnis, A. Mineral replacement reactions. *Reviews in mineralogy and geochemistry*, **70** (1), 87-124
593 (2009).

594 Putnis, A. Transient porosity resulting from fluid–mineral interaction and its consequences. *Reviews*
595 *in Mineralogy and Geochemistry*, **80** (1), 1-23 (2015).

596 Putnis, A., Moore, J., Prent, A. M., Beinlich, A., & Austrheim, H, 2021. Preservation of granulite in
597 a partially eclogitized terrane: Metastable phenomena or local pressure variations? *Lithos*, **400**,
598 106413 (2021).

599 Räss, L., Duretz, T., Podladchikov, Y. Y., & Schmalholz, S. M. M2Di: Concise and efficient
600 MATLAB 2- DS toke solvers using the Finite Difference Method. *Geochemistry, Geophysics,*
601 *Geosystems*, **18**(2), 755-768 (2017).

602 Rubie, D. C. Disequilibrium during metamorphism: the role of nucleation kinetics. *Geological*
603 *Society, London, Special Publications*, **138** (1), 199-214 (1998).

604 Rybacki, E., & Dresen, G. Dislocation and diffusion creep of synthetic anorthite aggregates.
605 *Journal of Geophysical Research: Solid Earth*, **105**(B11), 26017-26036 (2000).

606 Rybacki, E., & Dresen, G. Deformation mechanism maps for feldspar
607 rocks. *Tectonophysics*, **382**(3-4), 173-187 (2004).

608 Schmalholz, S. M., & Fletcher, R. C. The exponential flow law applied to necking and folding of a
609 ductile layer. *Geophysical Journal International*, **184**(1), 83-89 (2011).

610 Schmalholz, S. M., Moulas, E., Plümper, O., Myasnikov, A. V., & Podladchikov, Y. Y. 2D
611 Hydro-Mechanical-Chemical Modeling of (De) hydration Reactions in Deforming Heterogeneous
612 Rock: The Periclase-Brucite Model Reaction. *Geochemistry, Geophysics, Geosystems*, **21**(11),
613 e2020GC009351 (2020).

614 Schmid, D. W., & Podladchikov, Y. Y. Analytical solutions for deformable elliptical inclusions in
615 general shear. *Geophysical Journal International*, **155** (1), 269-288 (2003).

616 Schubnel, A., Brunet, F., Hilairet, N., Gasc, J., Wang, Y., & Green, H. W., 2013. Deep-focus
617 earthquake analogs recorded at high pressure and temperature in the laboratory. *Science*, **341**(6152),
618 1377-1380 (2013).

619 Schulte-Pelkum, V., Monsalve, G., Sheehan, A., Pandey, M. R., Sapkota, S., Bilham, R., & Wu, F.
620 Imaging the Indian subcontinent beneath the Himalaya. *Nature*, **435** (7046), 1222-1225 (2005).

621 Schulte-Pelkum, V., Monsalve, G., Sheehan, A. F., Shearer, P., Wu, F., & Rajaure, S. Mantle
622 earthquakes in the Himalayan collision zone. *Geology*, **47** (9), 815-819 (2019).

623 Shi, F., et al. Lower-crustal earthquakes in southern Tibet are linked to eclogitization of dry
624 metastable granulite. *Nature communications*, **9** (1), 1-13 (2018).

625 Spear, F. S., 1993, Metamorphic phase equilibria and pressure-temperature-time paths: Washington,

626 D.C., *Mineralogical Society of America Monograph* 1, 799 p.

627 Stünitz, H., & Tullis, J. Weakening and strain localization produced by syn-deformational reaction
628 of plagioclase, *International Journal of Earth Sciences*, **90**(1), 136-148 (2001).

629 Thielmann, M., Rozel, A., Kaus, B. J. P., & Ricard, Y. Intermediate-depth earthquake generation
630 and shear zone formation caused by grain size reduction and shear heating. *Geology*, **43** (9), 791-
631 794 (2015).

632 Thomas, M.Y., & Bhat, H.S. Dynamic evolution of off-fault medium during an earthquake: a
633 micromechanics based model, *Geophysical Journal International*, **214** (2), 1267–1280 (2018).

634 Ulven, O. I., Storheim, H., Austrheim, H., & Malthe-Sørensen, A. Fracture initiation during volume
635 increasing reactions in rocks and applications for CO₂ sequestration. *Earth and Planetary Science*
636 *Letters*, **389**, 132-142 (2014).

637 Vrijmoed, J. C., Podladchikov, Y. Y., Andersen, T. B., & Hartz, E. H. An alternative model for
638 ultra-high pressure in the Svartberget Fe-Ti garnet-peridotite, Western Gneiss Region, Norway.
639 *European Journal of Mineralogy*, **21**(6), 1119-1133 (2009).

640 Wain, A. L., Waters, D. J., & Austrheim, H. Metastability of granulites and processes of
641 eclogitisation in the UHP region of western Norway. *Journal of Metamorphic Geology*, **19**(5), 609-
642 625 (2001).

643 Wayte, G. J., Worden, R. H., Rubie, D. C., & Droop, G. T. A TEM study of disequilibrium
644 plagioclase breakdown at high pressure: the role of infiltrating fluid. *Contributions to Mineralogy*
645 *and Petrology*, **101**(4), 426-437 (1989).

646 White, R., Powell, R., Holland, T., Johnson, T., Green, E. New mineral activity–composition
647 relations for thermodynamic calculations in metapelitic systems. *J. Metamorph. Geol.* **32**, 261–286
648 (2014.).

649 Yamato, P., Duretz, T., & Angiboust, S. Brittle/ductile deformation of eclogites: insights from
650 numerical models. *Geochemistry, Geophysics, Geosystems*, **20** (7), 3116-3133 (2019).

651 Young, D. J., & Kylander-Clark, A. R. C. Does continental crust transform during eclogite facies
652 metamorphism?. *Journal of Metamorphic Geology*, **33** (4), 331-357 (2015).

653 Zertani, S., Labrousse, L., John, T., Andersen, T. B., & Tilmann, F. The interplay of Eclogitization
654 and deformation during deep burial of the lower continental crust—A case study from the Bergen
655 Arcs (Western Norway). *Tectonics*, **38** (3), 898-915 (2019).

656

657 **Data availability**

658 All numerical model outputs are available from the corresponding author upon request. They can
659 also be reproduced by using the scripts provided in supplementary materials.

660 **Code availability**

661 Matlab scripts for the analytical solution and the 1D model are provided in supplementary
662 materials. The 2D code is available here: <https://github.com/tduretz/MDOODZ6.0> (input file for the
663 2D reference model is given in supplementary materials). For further requests on the numerical
664 code please contact the authors.

665

666 **Acknowledgements**

667 P.Y. thanks the Institut Universitaire de France for financial support. We also thank Alexander
668 Webb and an anonymous reviewer for their comments and the editorial handling which contributed
669 to the improvement of the final version of the manuscript.

670 **Declaration of competing interest**

671 The authors declare that they have no known competing financial interests or personal relationships
672 that could have appeared to influence the work reported in this paper.

673

674

675 **Table 1** Parameters used in reference models

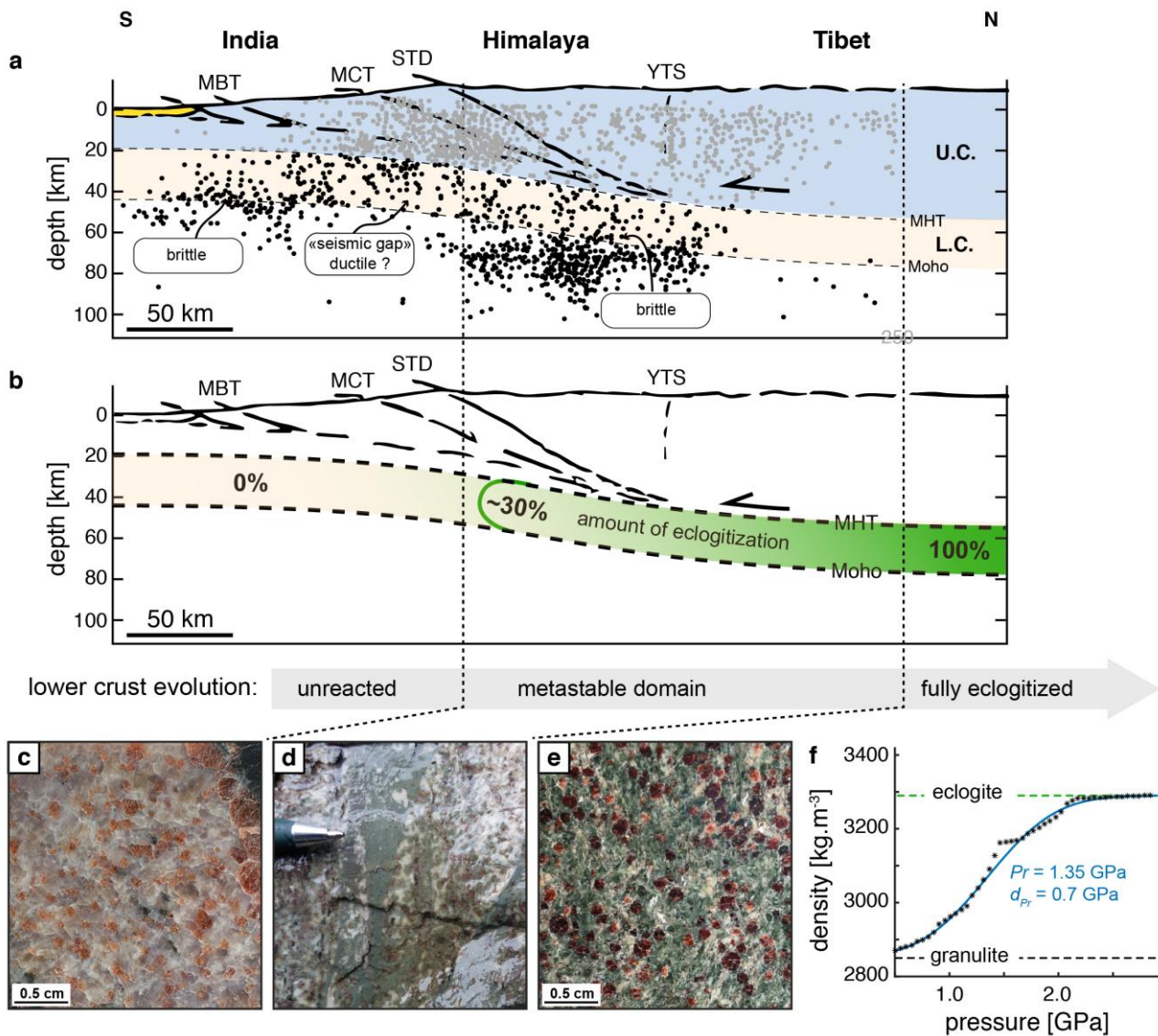
676

677

Symbol	Meaning	Unit	Value
1D reference model (without background strain rate and using linear viscosity)			
P_{BG}	Background pressure	GPa	2.0
P_r	Pressure of reaction	GPa	1.5
ΔP_m	Pressure overstepping ($P_{BG}-P_r$)	GPa	0.5
d_{Pr}	P_r standard deviation	GPa	0.7
ρ_1	Initial density (before transformation)	kg.m ⁻³	2850
ρ_2	Final density (after total transformation)	kg.m ⁻³	3250
t_k	Kinetic parameter*	s	3.1558×10 ⁹
K	Bulk modulus	GPa	80
G	Shear modulus	GPa	40
η	Viscosity	Pa.s	10 ²²
2D reference model (with background strain rate and visco-elasto-plastic rheologies)**			
$\dot{\epsilon}_{BG}$	Background strain rate	s ⁻¹	10 ⁻¹⁴
T_{BG}	Temperature	°C	680
A	Pre-exponential factor (dislocation creep)***	Pa ⁻ⁿ .s ⁻¹	5.0119×10 ⁻⁶
n	Exponent (dislocation creep)***	-	3
E_a	Activation energy (dislocation creep)***	kJ.mol ⁻¹	648
C	Cohesion	MPa	50
φ	Friction angle	°	30
η_{vp}	Viscoplastic viscosity	Pa.s	5 ×10 ¹⁸
C_p	Heat capacity	J.kg ⁻¹ .K ⁻¹	1050
k	Conductivity	W.m ⁻¹ .K ⁻¹	2.3

*see Supplementary Fig. 1 for more details **Parameters that are the same in both 1D and 2D model (i.e. elastic and metamorphic reaction properties) are not recalled for 2D reference model. ***Values from Rybacki and Dresen (2000) for anorthite dry.

678



681

682 **Fig. 1** (a) Cross-section in southern Tibet with seismicity datasets from Monsalve et al. 2006, Monsalve et al.

683 2009 and Schulte-Pelkum et al. 2019. Seismic events in the upper crust are plotted in grey. Deeper events are

684 in black. Abbreviations: U.C. = upper crust, L.C. = lower crust, MBT = Main boundary thrust, MCT = Main

685 Central Thrust, STD = Southern Tibet Detachment, YTS = Yarlung Tsangpo Suture, MHT = Main

686 Himalayan thrust. (b) Estimated amount of eclogitization of the lower crust for the same cross-section (after

687 Hetényi et al., 2007; 2021 and Schulte-Pelkum et al., 2005). c, d, e: Field photographs from Holsnøy

688 displaying progressive eclogitisation of lower continental granulite. (c) Untransformed granulite mainly

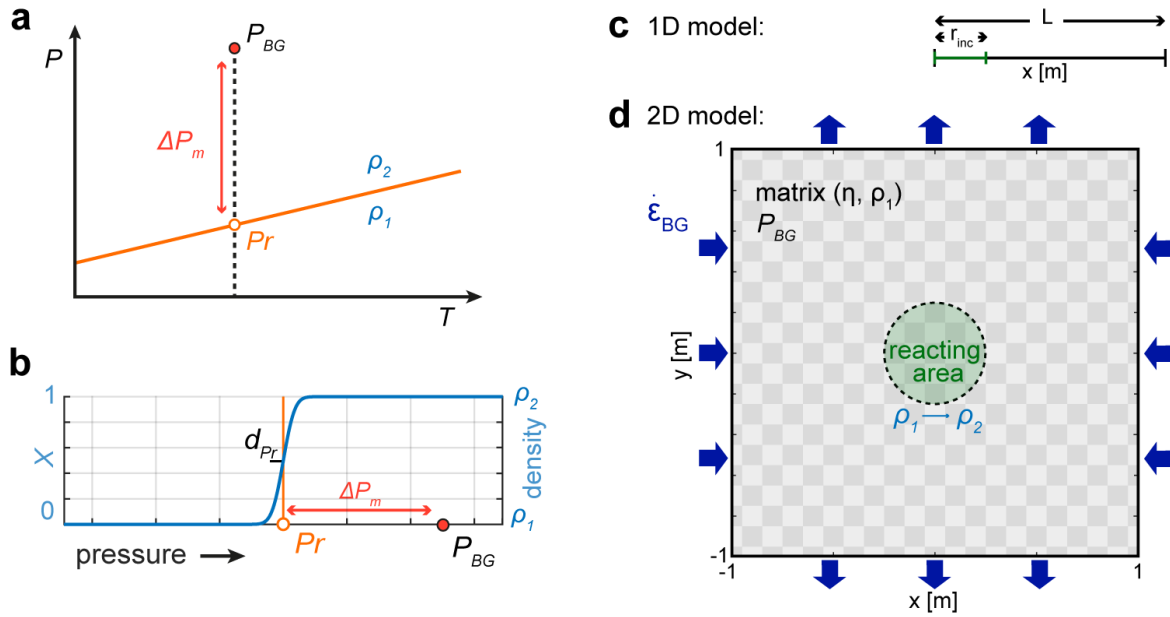
689 constituted by garnet, plagioclase and pyroxene (red, white and black minerals, respectively). (d) High-

690 pressure pseudotachylyte formed during eclogitization (Austrheim and Boundy, 1994; Bjørnerud and

691 Magloughlin, 2004). (e) Granulite fully transformed into eclogite with garnet (red), omphacite (green) and
692 zoisite-kyanite-quartz (yellowish assemblage). (f) Possible evolution of rock's density with pressure during
693 the granulite to eclogite metamorphic transformation. Black stars correspond to density data extracted from
694 Perple_X_6.9.1 (Connolly, 1990; 2009) at $T = 680^{\circ}\text{C}$ (see details in section 2.5.). Blue curve corresponds to
695 a possible fit of the density evolution using a cumulative distribution function with a mean pressure (P_r) of
696 1.35 GPa and a standard deviation (d_{P_r}) of 0.7 GPa as defined in Fig. 2b and considering reference densities
697 of 2850 kg.m^{-3} and 3290 kg.m^{-3} for granulite and eclogite, respectively.

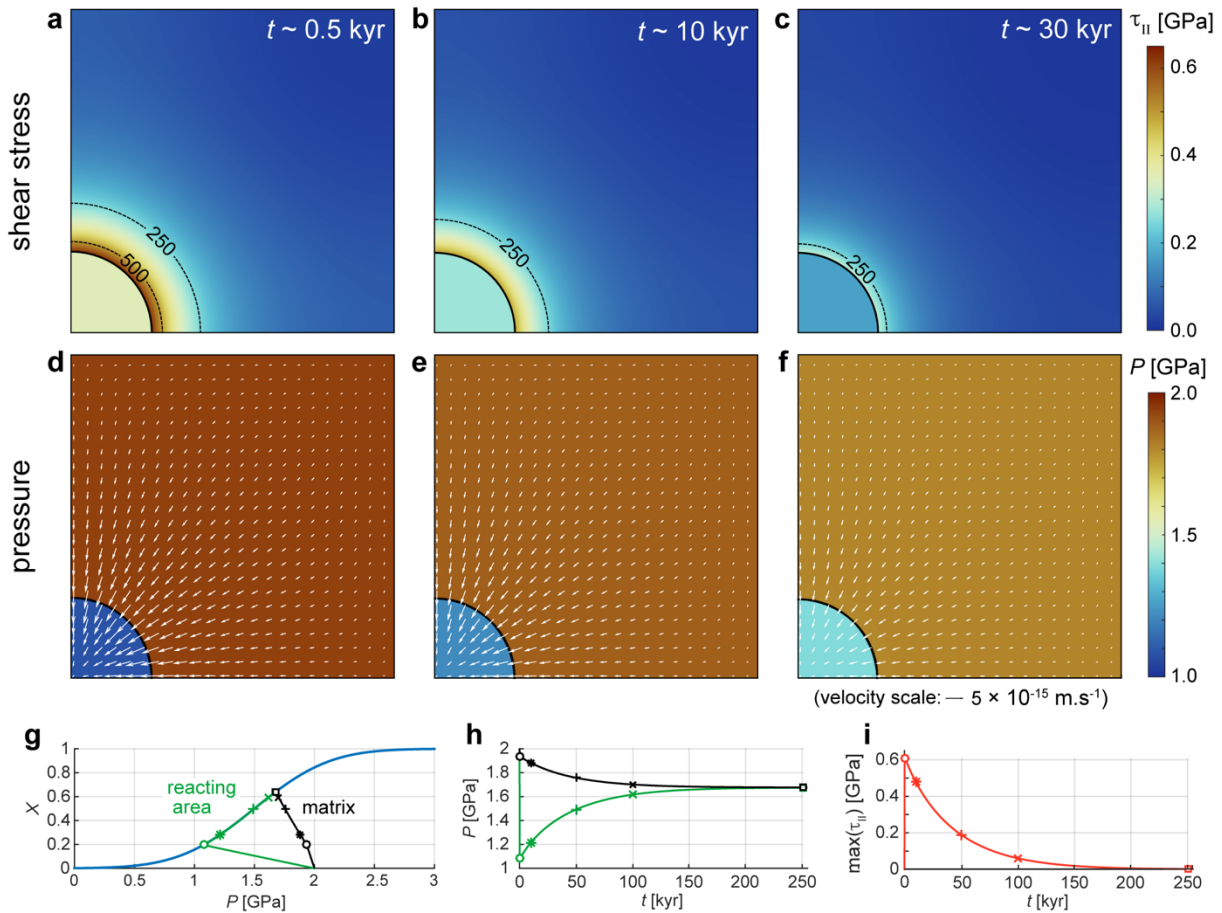
698
699

700 **Figure 2**
 701



702
 703 **Fig. 2** (a) Pressure (P) – temperature (T) diagram presenting a metamorphic reaction (orange line) associated
 704 with a density change (from ρ_1 to ρ_2). ΔP_m corresponds to the initial pressure overstepping, i.e. the difference
 705 between the background pressure (P_{BG}) and the pressure of the metamorphic reaction (P_r), for a fixed
 706 temperature. (b) Model of density evolution of a rock in thermodynamic equilibrium along the pressure path
 707 of Fig 2a. (dashed line). This model (blue line) corresponds to a cumulative distribution function centred on
 708 P_r with a standard deviation of d_{Pr} that controls the density change sharpness. It also reflects the progress of
 709 the reaction from $X = 0$ (unreacted material) to $X = 1$ (fully reacted material). (c) 1D model setup (see section
 710 2.3). L is the total length of the model. r_{inc} is the part where metamorphic reaction (i.e. density change)
 711 occurs. (d) 2D model setup with background strain rate ($\dot{\epsilon}_{BG}$) as boundary conditions (dark blue arrows, see
 712 section 2.4). Green inclusion (reacting area) has the same material properties as the matrix, but density
 713 change associated with metamorphic reaction is activated in this domain.

714

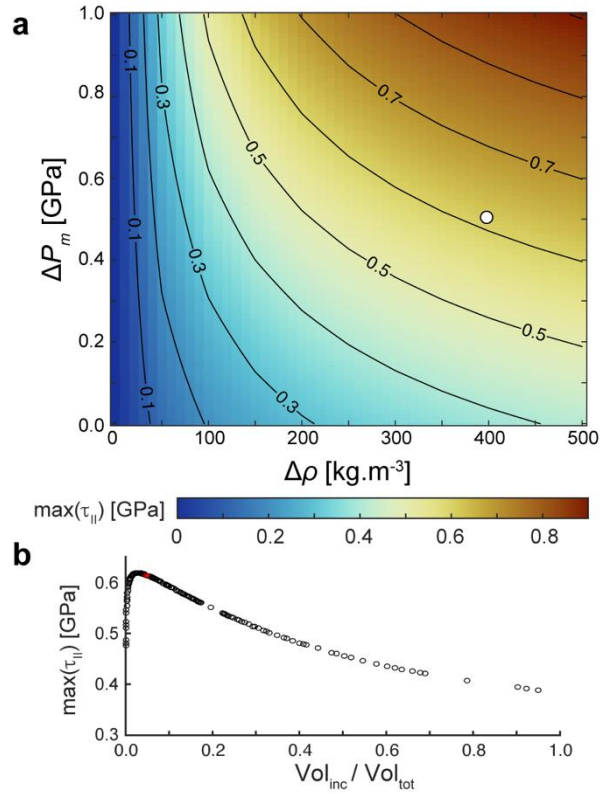


716

717 **Fig. 3** Evolution of shear stress (a-c), pressure and velocity field (d-f) for the 2D reference model with time
 718 (top-right quarter of the model only). Parameters used are those of the 1D reference model (see Table 1). For
 719 comparison, results from the 1D model (see section 2.3. and Table 1 for parameters) are presented in (g) to
 720 (i) as follows: (g) Evolution of pressure with reaction progress (X) in matrix (black line) and in the reacting
 721 area (green line). Circle, asterisk, plus and multiplication symbols corresponds to different times (0.5, 10, 50,
 722 100 and 250 kyrs, respectively). Blue line is for a rock in thermodynamic equilibrium. (h) Evolution of
 723 pressure with time (t) for matrix (black line) and reacting area (green line). (i) Evolution with time of
 724 maximum of shear stress ($\max(\tau_{II})$) recorded in the matrix.

725

726



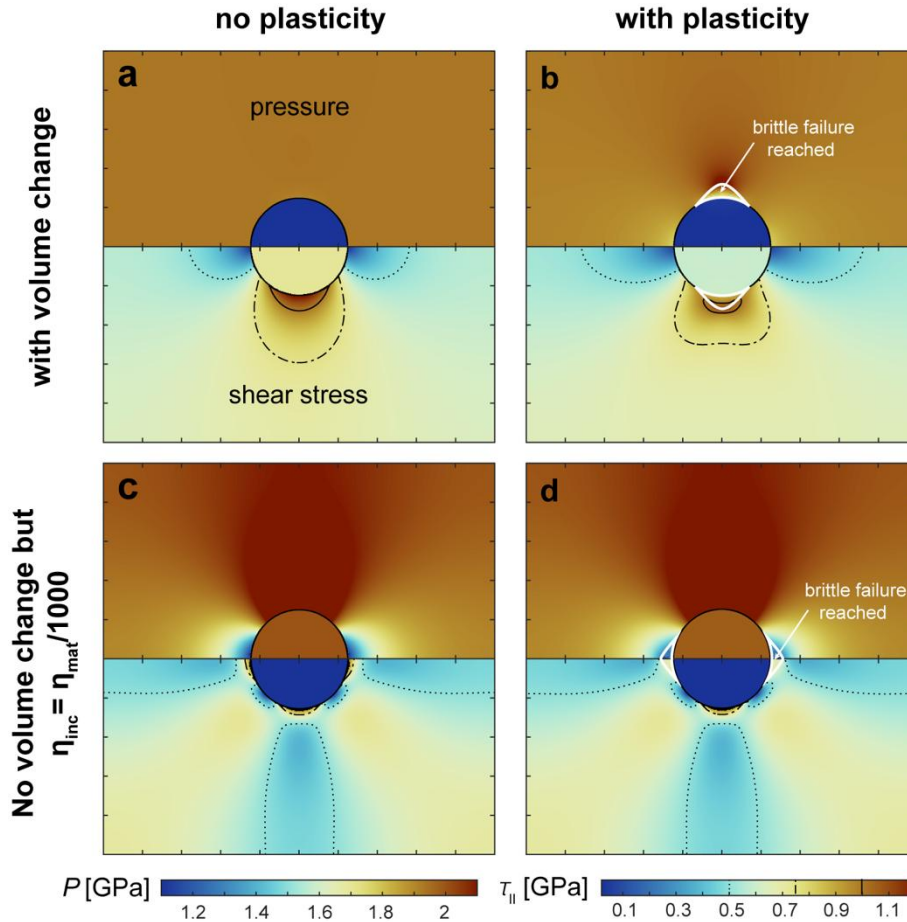
728

729 **Fig. 4** Shear stress generated by volume change. (a) Colourplot of maximum of shear stress, $\max(\tau_{II})$,
 730 recorded in the matrix as a function of degree of overstepping (ΔP_m) and density change associated to the
 731 metamorphic reaction ($\Delta\rho$). White dots correspond to the reference models presented in Fig. 3 (peak of
 732 $\max(\tau_{II})$ in Fig. 3i). (b) Influence of the initial size of the reacting area on the obtained maximum shear
 733 stress. Red star corresponds to result obtained in reference model (i.e. with $r_{\text{inc}} = 0.25$ m and $L = 2$ m).

734 $\text{Vol}_{\text{inc}}/\text{Vol}_{\text{tot}} = \pi r_{\text{inc}}^2/L^2.$

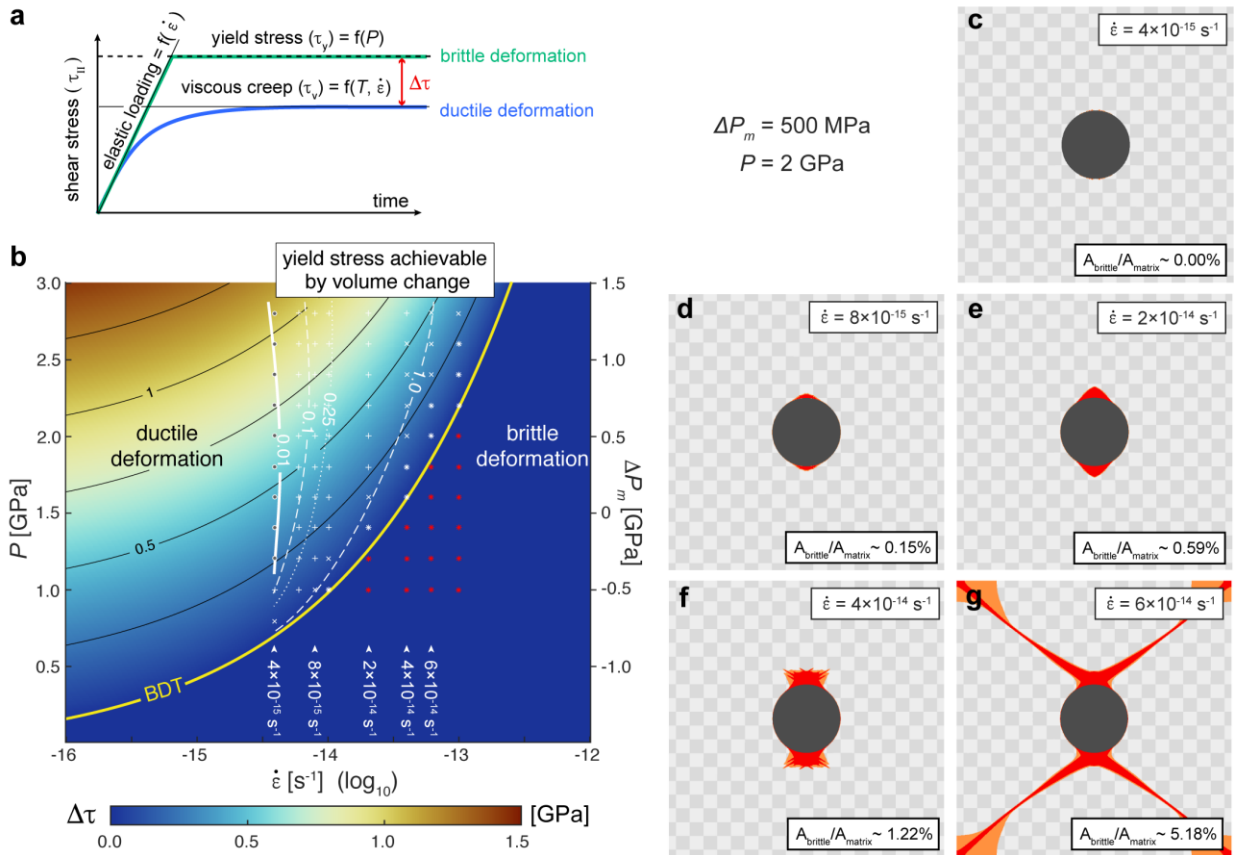
735

736



738

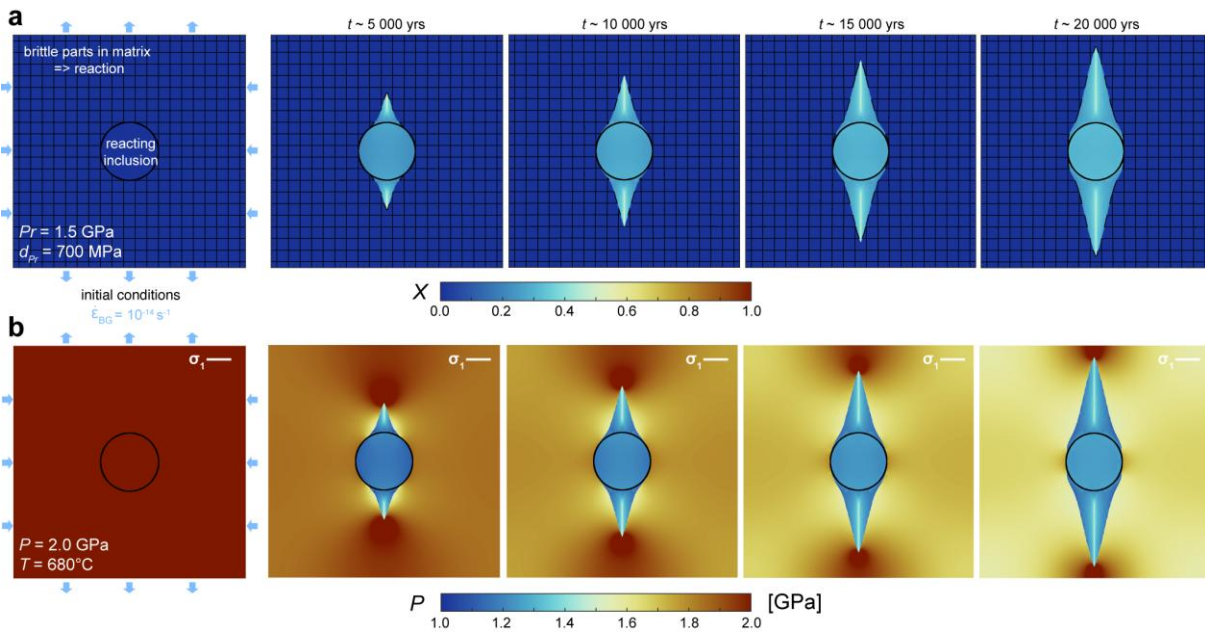
739 **Fig. 5** Volume change vs. viscosity contrast under pure shear deformation. Results are extracted from the 2D
 740 model (see section 2.4. and Table 1 for parameters) at $P_{BG} = 2$ GPa , $T = 680^\circ\text{C}$ and $\dot{\epsilon}_{BG} = 10^{-14} \text{ s}^{-1}$ after $t =$
 741 500 yrs. Each plot displays two panels as follows: (top) pressure field (bottom) shear stress (i.e. second
 742 invariant of the stress tensor) field. Plasticity is switched-off for models (a) and (c) and activated for models
 743 (b) and (d). In (a) and (b), densification is activated in the reacting inclusion ($\Delta\rho = 400 \text{ kg.m}^{-3}$; $P_r = 1.5$ GPa;
 744 $d_{Pr} = 700$ MPa) but inclusion and matrix have the same material property (Table 1). Viscosity present a stress
 745 exponent ($n=3$). In contrast, in (c) and (d), volume change due to the reaction is switched-off and the only
 746 difference between the inclusion and the matrix corresponds to a viscosity ratio (reference viscosity in the
 747 inclusion is 10^3 times weaker than in the matrix, and $n=3$). White contours delimitate the parts of the matrix
 748 that reached the yield stress and have undergone brittle failure.



751
752
753
754 **Fig. 6** Overstepping and strain rate effects on brittle-ductile transition. (a) Loading curves for a visco-elasto-
755 plastic material undergoing ductile deformation (in blue) and frictional deformation (in green). $\Delta\tau$ is the
756 difference of shear stress (τ_{II}) between τ_y (yield stress value) and τ_v (viscous shear stress). (b) Values of $\Delta\tau$ in
757 the P vs. $\dot{\epsilon}$ diagram for anorthite dry (see parameters in Table 1) at $T = 680^\circ C$. Symbols correspond to
758 simulations performed using the 2D model (see section 2.4.) at $T = 680^\circ C$ for $P_r = 1.5$ GPa and $d_{pr} = 700$
759 MPa. Results (extracted after $t = 1000$ yrs) allows to define the ratio between the amount of matrix area that
760 reached the yield stress ($A_{brittle}$, red colours in (c-g)) and the total amount of matrix material (A_{matrix}). Areas
761 depicted in orange and red correspond to zones that reached a plastic strain of 10^{-5} and 10^{-3} , respectively.
762 White dashed lines in (b) correspond to isocontours of this ratio (in %). BDT = Brittle-ductile transition. Five
763 different symbols are used to group the similar results: Grey dots are used for models similar to (c), i.e.
764 where brittle features are not significant; + signs are used for models as in (d) and (e), x signs are used when
765 shear zones start to propagate as in (f); stars are used when well developed shear zones propagate as in (g);
766 red stars correspond to models belonging to the brittle domain as illustrated in Supplementary Figure 5.

767

768 **Figure 7**



769
770

771 **Fig. 7** Models of transformation propagation. In these models, the parts of the matrix that reached an
772 accumulated plastic strain of 10^{-3} (i.e., red area from Fig.6e) are allowed to react (i.e. same properties as the
773 initial inclusion are affected to them). (a) Reaction progress with time (b) Pressure evolution. Black contour
774 corresponds to the initial position of the reacting area. White line shows the orientation of the maximum
775 principal stress (σ_1) applied on the model.

776

777